Nicoleta Herzog[1]
Institute for Energy Systems and Fluid-Engineering,
School of Engineering,
Zurich University of Applied Sciences,
Winterthur 8400, Switzerland

Alexander Weber[2]
Institute for Energy Systems and Fluid-Engineering,
School of Engineering,
Zurich University of Applied Sciences,
Winterthur 8400, Switzerland

Armin Purea
Bruker BioSpin GmbH,
Rheinstetten 76287, Germany
e-mail: Armin.Purea@bruker.com

David Osen
Bruker BioSpin GmbH,
Rheinstetten 76287, Germany
e-mail: David.Osen@bruker.com

Benno Knott
Bruker BioSpin GmbH,
Rheinstetten 76287, Germany

Frank Engelke
Bruker BioSpin GmbH,
Rheinstetten 76287, Germany
e-mail: Frank.Engelke@bruker.com

Dirk Wilhelm[3]
Professor
Institute of Applied Mathematics and Physics,
School of Engineering,
Zurich University of Applied Sciences,
Winterthur 8400, Switzerland
e-mail: Dirk.Wilhelm@zhaw.ch

Ultra Low Temperature Microturbine for Magic Angle Spinning System

We investigate the fluid dynamics of a microturbine system that is applied in a device for chemical and biological analysis—a so-called magic angle spinning (MAS) nuclear magnetic resonance (NMR) probe. The present system is utilized in a wide temperature range from 45 K to 293 K. Pressurized air, nitrogen, or helium are used to drive a Pelton type microturbine. This turbine is mounted on a MAS rotor with a diameter between 0.7 mm and 3.2 mm. The rotor system is equipped with a pressurized gas bearing that is operated by the same gas species as the turbine. Computational fluid dynamics (CFD) simulations have been performed and compared with fluid dynamics measurements of the MAS system for different diameters, temperatures, and spinning rates between 23 kHz and 120 kHz. To our knowledge, this work is the first comprehensive CFD and experimental study of such a wide temperature range that has been carried out for microturbines with pressurized gas bearings. The results show good agreement between measurements and CFD simulations with appropriate (real) gas models, i.e., the ideal gas model for air at room temperature, Peng–Robinson model for nitrogen at 105 K, and ideal gas model for helium at 45 K. [DOI: 10.1115/1.4053746]

1 Introduction

During the last years, microfluidics has gained increasing attention for various applications such as microfluidic mixers [1], cavity driven microfluidic systems [2], or microfluidic sensors [3], for an overview we refer to Sharp [4]. In particular microturbines with rotor diameter in the range of less than 1 mm to 10 mm are an interesting category of microfluidic systems, see, e.g., Refs. [5–9]. Lee et al. [9] presented a plant-on-a-chip microsteam turbine fabricated on a silicon base and delivering 4.7 W of mechanical power. In general, microturbines have been employed for power generation in a wide range of less than 1 W to 100 W [10–15]. In the literature rotor speed of 100,000 revolutions per minute (about 1.6 kHz) up to more than one million revolution per minute can be found (e.g., Ref. [5]).

In this work, we consider a microturbine that is employed in nuclear magnetic resonance (NMR) spectroscopy. NMR spectroscopy is a widely used analytical method in biology, chemistry, and material science. It has the capability to give deep insight into the molecule structure (see, e.g., Refs. [16–18]). The basic principle of NMR relies on placing the sample of interest in a very strong static magnetic field (1–28 Tesla) that aligns the nuclear spins of the sample. Simultaneously, a radio frequency (RF) field is irradiated onto the sample in order to manipulate the nuclear spins. The reaction of the spins to the RF field is measured in form of a spectrum revealing information about the molecule structure of the sample. The enhancement of spectral quality is a very important optimization factor in NMR spectroscopy. Herein the main parameters are the signal-to-noise ratio (SNR) and the width of the spectral lines. In NMR, nuclear spins are aligned along or against the static magnetic field, leading to different energy states. Since the population difference between these energy states is very small (about one ten thousandths of all nuclear spins), NMR is a rather insensitive method. Consequently, an increase of the signal-to-noise ratio is a major research and development direction in NMR instrumentation.

In general, two NMR methods can be distinguished, liquid and solid state NMR. In liquid NMR, the sample is dissolved, for example, in water or organic solvents, and measured in a sample

[1]Present address: CompuGroup Medical Deutschland AG, Maria Trost 23, D-56070 Koblenz, Germany.
[2]Present address: OST Ostschweizter Fachhochschule, IET Institut für Energietechnik, CH-8640 Rapperswil SG, Switzerland.
[3]Corresponding author.

Contributed by the Fluids Engineering Division of ASME for publication in the Journal of Fluids Engineering. Manuscript received September 13, 2021; final manuscript received January 22, 2022; published online March 8, 2022. Assoc. Editor: Arthur Favrel.

tube of 1 mm–7 mm diameter. In solid-state NMR, the sample is usually powdered and placed in a sample container for NMR examination. Due to a quantum mechanical coupling phenomenon, solid-state samples produce very wide spectral lines and consequently low quality spectra. It is well known that spinning the solid state sample under the so-called magic angle of 54.7 deg relative to the static magnetic field direction averages out this quantum mechanical coupling, resulting in narrow lines. However, the line width is a function of the rotation speed and therefore in practical applications 1000 up to about 100,000 revolution per second (1–100 kHz) are employed. The sample is filled in a sample container, the so-called rotor. Common rotor diameters are 0.7 mm, 1.3 mm, or 3.2 mm. This rotor is equipped with a tiny Pelton type turbine on its top driven by air, nitrogen, or helium. The so-called magic angle spinning (MAS) system encompasses also a pressurized gas bearing that is operated with the same gas as the turbine. The principle of the MAS system and some theoretical considerations are given in Refs. [19–24].

The optimization directions in developing MAS systems are further increase of the revolutions per second [25] and increase of SNR. Consequently, the microturbine and the gas bearing system have been subjected to intensive research and development work. In the past, experimental testing in an empirical manner has played an important role, whereas computational fluid dynamics (CFD) analysis is not very wide spread in the design of MAS systems, cf. [24–27]. Recently, Sesti et al. [26] reported CFD simulations of NMR systems at very low temperature (i.e., 6 K). Also, spherical rotor geometries were proposed and investigated [28–30]. Wilhelm et al. [24] reported one of the first CFD simulation study of a MAS system. Herein it is shown that the power generated by the microturbine is in the range of 6 W and the efficiency is about 20%, which is rather low compared to industrial Pelton turbine systems for power generation [31,32]. Herzog et al. [27] investigated the MAS system in more detail employing CFD simulations compared with experimental measurements. They contributed to the optimization directions for the air propelled turbine design for the rotation speed of 23 kHz to 67 kHz. Moreover, sensitivity to fabrication tolerances is studied for the tiny turbines of 1.3 mm diameter in that work.

As mentioned before, the increase of the SNR is one major optimization direction of nuclear magnetic resonance spectroscopy. In the last years dynamic nuclear polarization (DNP) methods have gained significant interest [33,34], although the method is not new (for a review see Ref. [35]). The basic idea of DNP is to polarize the electron spin of the rotating sample by radiation of high frequency microwaves of about 200 GHz at a low sample temperature of about 80–110 K employed. Rosay et al. [33] use a spinning frequency of 8–12 kHz at a sample temperature of 97–103 K, employing cryogenic nitrogen gas as drive, cooling, and bearing medium. To further increase the SNR, a research group at Grenoble [36] has developed an ultralow temperature DNP-MAS system that utilizes cooled helium gas as drive, cooling, and bearing medium. Lee et al. [36] achieved MAS spinning frequencies of 13 kHz at 36 K employing a 3.2 mm MAS rotor system. The combination of ultralow temperature DNP with moderate sample spinning lead to a significant enhancement of the SNR by a factor of more than 300.

The scope of this paper is to provide an in-depth analysis of a microturbine system equipped with a gas bearing for a large temperature range of 45–293 K. The turbine and bearing system is driven by three different media, i.e., either helium, nitrogen, or air. CFD simulations utilizing the tool package OpenFOAM employing ideal gas and real gas models are compared in this work. Special emphasize is laid on fluid dynamic modeling of the microturbine.

The paper is structured as follows. In Sec. 2 we introduce a MAS turbine system with its flow geometry and relevant characteristics. Furthermore, we focus on the numerical methodology, the mesh generation, and the considered fluid parameters and boundary conditions in this section. In Sec. 3 we discuss the results, followed by a conclusion in Section 4.

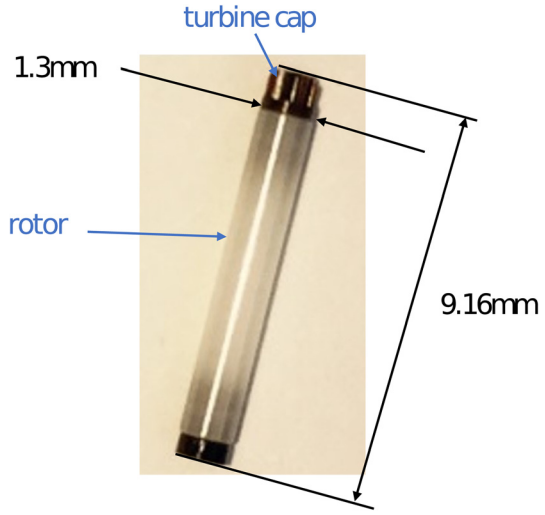

Fig. 1 Rotor with turbine cap mounted on top

2 Case Description and Numerical Methodology

In magic angle spinning NMR, we consider the following basic configuration: a MAS rotor containing the NMR sample, which is rotated with the frequency f in the range of spinning rates of 5 kHz–120 kHz. The rotor is driven by a turbine that is mounted on the top end of the rotor (the so-called turbine cap, see Fig. 1). The rotor is positioned by two radial gas bearings. The principle of a typical MAS turbine configuration is shown in Figs. 2 and 3.

Magic angle spinning probe heads are equipped with two separate gas flow supplies, i.e., drive flow and bearing flow. The two radial gas bearings are fed through five nozzle flows, each. Herein, the bearing flow passes through the nozzles impinges onto the rotor, and flows either toward the center of the rotor or mixes to a smaller fraction with the turbine fluid flow. The turbine fluid flow passes the inlet plane, flows through a pipe, and is hereafter distributed into five to seven circumferential pipes. The gas flow exits the rotor chamber in the upward and downward direction and reaches the outlet bottom or top, respectively. The principal system as sketched in Figs. 2–4 has been previously introduced by Herzog et al. [27].

In our study different rotor diameters were considered, namely, 3.2 mm, 1.3 mm, and 0.7 mm rotor systems. Depending on its diameter, the rotor is rotated with the frequency f in the range of spinning rates between 5 kHz and 120 kHz. The smaller the diameter is, the higher is the reached spinning rate.

2.1 Numerical Methodology. Since the MAS system consists of rotating and static parts, specific numerical approaches are needed. The steady-state domain, the stator, is formed by the housing and includes the port for the drive pressure (inlet) and the outlet regions, where the gas flow exits the system. The rotating domain is composed of the bladed turbine cap, and the rotor revolves with a certain angular velocity with respect to the system z-axis (see Fig. 2).

For providing quantitative results, the aerodynamic forces and torques acting on the turbine were evaluated from the simulation data. The axial force acting on the turbine was found to act downward in the negative z-direction and it plays a role in directing and stabilizing the rotor system. The x- and y-force components are important for the rotor stability, because these components may generate a tilting movement that destabilizes the rotor. The momentum component around the rotation axis z is the drive torque M_z. The other two momentum components around the x- and y-axis corresponding to the tilt moments are usually considered by

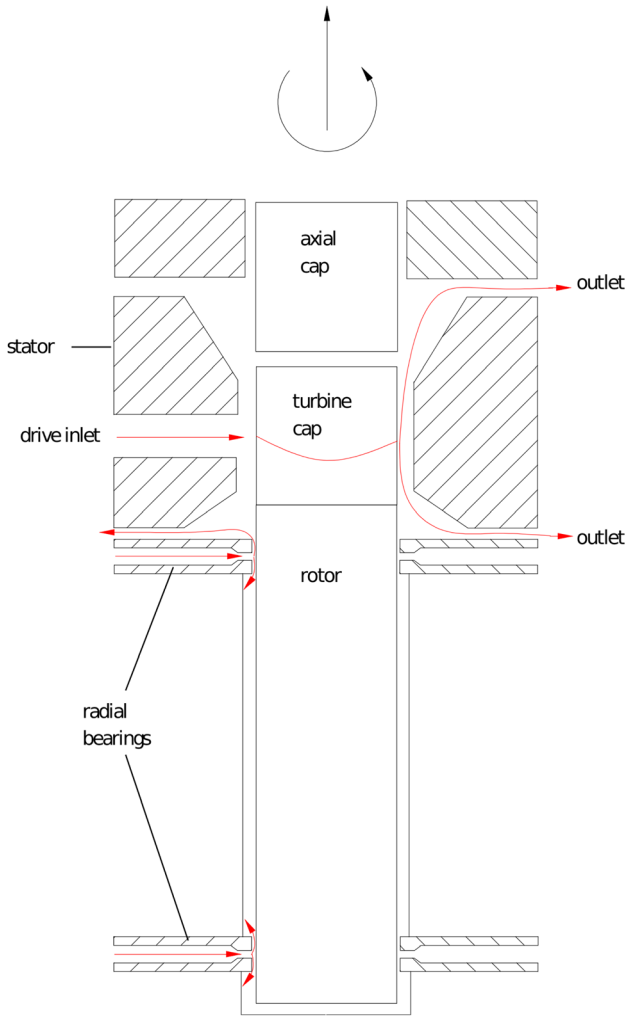

Fig. 2 Sketch of the MAS rotor system with turbine and radial bearings. The rotor is rotating around the *z*-axis with an angular rotation frequency $\omega = 2\pi f$. Figure adapted from Herzog et al. [27].

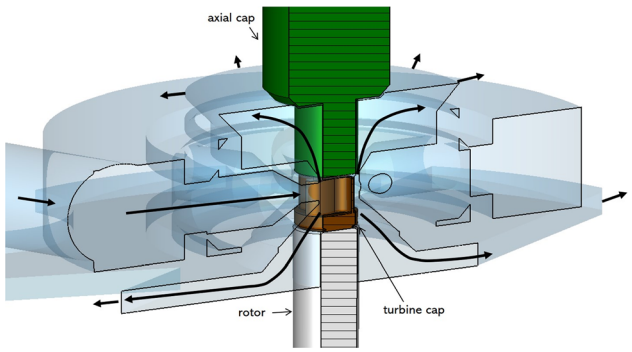

Fig. 3 View of the 1.3 mm rotor and stator flow region. The drive gas is supplied from the inlet and afterward distributed into the drive nozzles, then driving the turbine and leaving through the various outlet planes. Figure adapted from Herzog et al. [27].

a stability analysis of the gas bearing, which is beyond the scope of this work.

The employed numerical methodology is based on the multiple reference frame (MRF) method, also known in turbomachinery as the frozen rotor approach. In the rotating part, the Navier–Stokes equations are solved in the associated relative frame

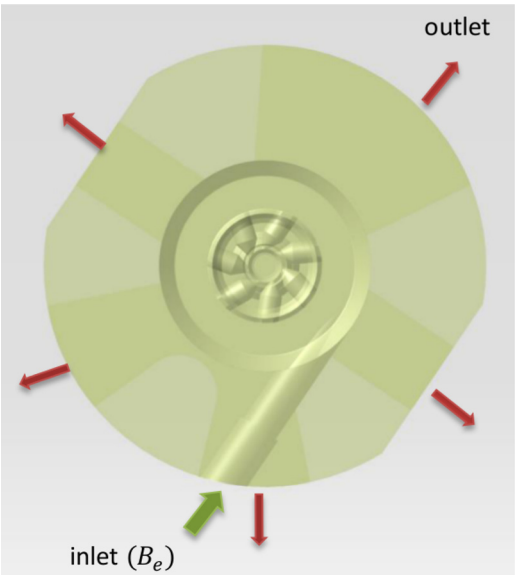

Fig. 4 Top few of the turbine flow domain. Figure adapted from Herzog et al. [27].

$$\frac{\partial(\rho \mathbf{u}_r)}{\partial t} + \nabla \cdot (\rho \mathbf{u}_r \mathbf{u}_r) + 2\rho\boldsymbol{\omega} \times \mathbf{u}_r + \rho\boldsymbol{\omega} \times (\boldsymbol{\omega} \times \mathbf{r}) = -\nabla p + \nabla \cdot (\mu \nabla \mathbf{u}_r) \tag{1}$$

Two additional acceleration terms occur in this momentum equation, namely, the Coriolis and the centrifugal term. In the stator part, the corresponding equations in a steady-state frame

$$\frac{\partial(\rho \mathbf{u})}{\partial t} + \nabla \cdot (\rho \mathbf{u}\mathbf{u}) = -\nabla p + \nabla \cdot (\mu \nabla \mathbf{u}) \tag{2}$$

are considered. Here pressure, density, and dynamic viscosity are denoted by p, ρ, μ, respectively. The velocity relative to the rotating frame ($\mathbf{u}_r$) is defined as the difference between the absolute velocity $\mathbf{u}$ and the peripheral velocity

$$\mathbf{u}_r = \mathbf{u} - \boldsymbol{\omega} \times \mathbf{r} \tag{3}$$

where $\omega = 2\pi f$ is the angular velocity and f is the rotation frequency. The information between steady-state and rotating zones is transferred through the arbitrary mesh interface at each iteration step. This interface is required exclusively for the numerical simulation to connect the two computational domains and has no physical meaning. At these interfaces between the two references frames a velocity steady-state flow condition is applied which assumes the same absolute velocity on both sides of the interface. In an inertial (nonaccelerating) coordinate system the flow around the rotating parts, such as the blades of the turbine, appears always unsteady due to the periodicity implied through the finite number of blades. Despite of the periodic sweeps the flow around the turbine can reach a stationary condition. For a rotating (noninertial) coordinate system fixed on the rotor, the flow is usually steady relative to the rotating frame.

When performing unsteady simulations, adding unsteady terms to all the governing equations of the MRF approach Eqs. (1) and (2) is not sufficient. In agreement with Ref. [37] the usage and the physical meaning of such results are questionable for transient simulations. Generally, more meaningful results for unsteady rotational flows are yielded by the sliding mesh method (SMM) for which the meshes and the geometry remain unchanged. The sliding mesh method allows adjacent grids to slide relative to each other along the interface surface, whereas the coupling between the two regions is achieved by interpolating the flow variables on the cell faces.

In our previous paper [27] both the MRF and the SMM approach were validated by performing three-dimensional simulations of the microturbine system. For steady-state simulations, the main problem was to calculate physical variable values which are independent of the rotor position relative to the nozzles. Therefore, three blade turbine positions at 0 deg, 30 deg, and 60 deg counterclockwise relative to the nozzles were considered. Individual and averaged values over the three angular positions of the forces and torques acting on the turbine were determined with the steady-state MRF approach. Small differences in the flow patterns lead to unequal pressure distribution on the turbine surface, which include small variances in the force and torque values. However, the test results carried out for the MAS 1.3 mm turbine systems at a rotation frequency of 23 kHz show for the averaged driven torque a percentage deviation of 0.22% from the results without averaging. In order to ensure that the averaging over the three rotor positions by steady-state simulations leads to the same result as the average over one revolution of a transient simulation, tests were performed with an unsteady solver based on the SMM approach. The test results show a percentage deviation of 0.5% in the transient simulation from the steady-state results without averaging. Since the discrepancies between the results are extremely small and the unsteady simulations lead to an increase of computational time by a factor of 5.5 compared to the combined calculation time of the three steady-state cases, the steady-state case with blade turbine positions at 0 deg relative to the nozzles was chosen for providing the results of this work.

For solving the set of the model equations the open source C++ library OpenFOAM version 2.3.1 was used (see, e.g., Ref. [38]). This CFD package provides specifically adapted solvers for given flow problems, including the MRF and the SMM technique. Due to the high contraction of the jet nozzles, the fluid can reach transonic and supersonic velocities, especially near the rotor blades. Therefore, the compressible flow equations coupled with the specific gas equation were solved. The *rhoSimpleFoam* module was considered as most suitable to perform simulation of the steady-state flow in the microturbine with the MRF approach. This application includes a pressure-based solver in which the momentum and continuity equations are solved simultaneously and the energy equation is put off until after the pressure correction step. When rapid changes in material properties take place, density-based solvers in which the momentum, continuity, and energy equations are solved together and the pressure field is computed from the equation of state are recommended, due to their better accuracy in trans-/supersonic regions. However, as long as the method remains stable, a pressure-based solver is a reasonable approach also for supersonic flows. To improve the stability, pressure relaxation was inserted for the used pressure-based applications. Moreover, supersonic regions can occur in the MAS system only locally near the rotor blades. In order to avoid any doubt, simulations with a density-based application were also carried out, as mentioned in Ref. [27], and no differences in the flow fields were found. The steady-state simulations were mainly carried out by choosing upwind discretization for the advection terms and a linear scheme for the gradient terms. The minimum residual criterion was specified to 10^{-5} for all flow variables, namely, velocity u, pressure p, and enthalpy h.

2.2 Turbulence Modeling. Another question posed was whether turbulence modeling is necessary for the simulation process. For that certain test simulations of a MAS 1.3 mm system at its maximal rotational frequency of 67 kHz were performed without turbulence model and with commonly used models like *komegaSST, komegaSST* for low Reynold numbers, and the *v2f model*. As concluded in Ref. [27] when using turbulence modeling the deviations in the momentum components are negligible especially for the drive torque. Initial calculations have shown that the Reynolds number at key locations, like pipe inflow, inflow spiral, largest ducts size, and nozzle exit, do not extend beyond turbulence transitional values. Only in the bottom outlet area at the turbine shaft, the flow reaches supercritical conditions. The resulting aerodynamic forces and torques on the turbine as well as the flow fields do not differ significantly when using turbulence modeling compared to the laminar solution. Due to the small differences for the torque components and the Reynolds numbers which are not completely located in the turbulent regime, all simulations of this work were performed without turbulence modeling. This was done also to avoid additional numerical diffusion introduced by turbulence models and because the mesh was sufficiently refined to resolve the flow fields.

2.3 Grid Generation. The grid generation of this paper is based on the methods of Herzog et al. [27]. The computational mesh for the performed microturbine simulations consists of two parts: the stator mesh and an inner rotor mesh. Three interface surfaces were needed to couple the two regions, one between the turbine's top surface and the casing, another on the side of the turbine between the blade tips and the casing where the nozzles enter the turbine area, and a third interface in the bottom region of the turbine. The locations of the interfaces were selected carefully to avoid numerical distortion of the results due to the presence of these interfaces and to ensure appropriate use of the sliding mesh approach.

Computational meshes are generated for two cases, the 1.3 mm turbine system and the 0.7 mm turbine system. For the 1.3 mm turbine system, structured hexahedron grids with a total number of 2,236,727 nodes and 2,376,561 cells, 30% of which are located within the rotor, were generated with the mesher ICEM-CFD version 15.0 of ANSYS. For the 0.7 mm turbine system, we also used structured hexahedron grids with a total number of 3,724,783 nodes and 3,523,440 cells. Figure 5 shows the grids employed for our 1.3 mm and 0.7 mm simulations. A cut through the grid on the nozzle level is given in Figs. 5(*c*) and 5(*e*) for the 1.3 mm and the 0.7 mm turbine systems, respectively. The near-wall regions are refined to resolve the boundary layer in the regions where the flow is accelerated because of the contraction of the nozzles. In order to compute the aerodynamic forces, a high quality mesh, especially in the surface region, is very important. The present grids are generated in a process of careful refinement studies. A detailed few meshes employed for the two cases, i.e., 1.3 mm turbine and 0.7 mm turbine, are given in Figs. 5(*c*), 5(*d*), 5(*e*), and 5(*f*), respectively. An enlargement of the mesh refinement at the blade tip region illustrates the high quality of the grid, see Fig. 5(*f*). The grids contain cells with edge lengths between 0.03 mm and 0.7 mm in the stator part and a local refinement in the rotor region down to 0.16 μm. Note that the 1.3 mm turbine has four blades and seven inlet tubes, while the 0.7 mm turbine has five blades and eight inlet tubes.

2.4 Boundary Condition. For driving the microturbine three different fluids at specific inflow temperatures as shown in Table 1 are used. Air is entering the system at room temperature of 293 K, helium enters the system at about 45 K and nitrogen at about 105 K. Air and helium generally obey the ideal gas equation of state, but for nitrogen at 105 K real gas effects have to be considered.

Even though the investigated MAS system is a pressure driven flow problem, a mass flux inlet boundary condition was defined for the velocity to ensure the numerical stability of the simulation. At the inlet, a Dirichlet boundary condition was set for the temperature by assuming a uniform temperature of 293 K (ca. 20 °C) for the air flow, 45 K in case of helium driven system, and 105 K to 118 K for nitrogen. In the following, we indicate the nitrogen case by 105 K, for simplicity of the notation. The pressure was set to a Neumann condition by defining a zero gradient condition on the inlet patch which means that the gradient perpendicular to the inlet patch is set to zero and the pressure is obtained by the velocity field. Both outlet regions (top and bottom) were set to ambient

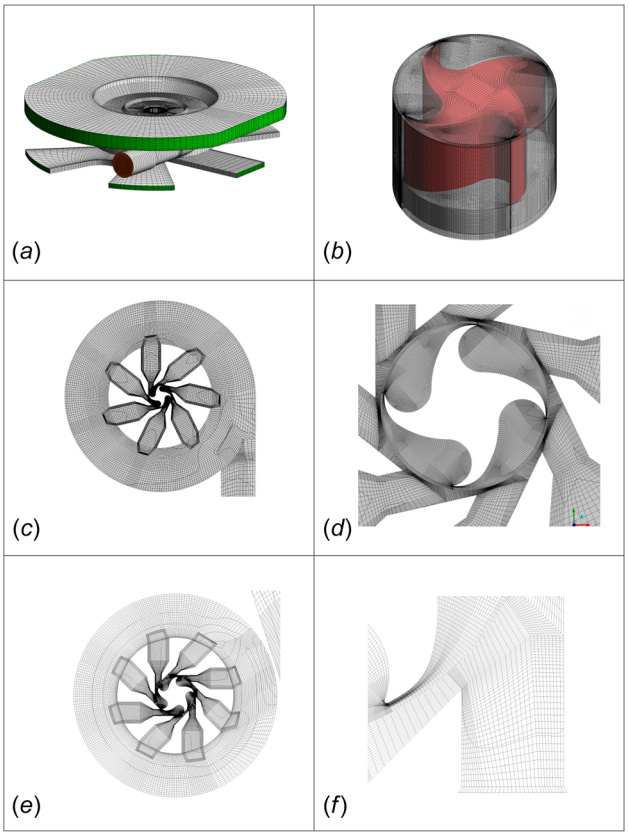

Fig. 5 Computational domain of hexahedron grids; 1.3 mm turbine system shown in (*a*)–(*d*), 0.7 mm turbine system shown in (*e*) and (*f*). (*a*) Entire simulation domain, (*b*) turbine rotor with mesh, (*c*) horizontal cut through 1.3 mm turbine system, (*d*) turbine grid, (*e*) horizontal cut through 0.7 mm turbine system, and (*f*) enlargement of blade tip (0.7 mm turbine system).

pressure conditions by defining a constant value of 1 bar. To prevent back flow and related numerical instability in the outlet area an *inletOutlet* condition was imposed for the velocity field. Since the outlet is regarded as adiabatic, a zero gradient condition was specified for temperature. At the system walls, the simple no-slip condition was applied. Furthermore, all walls are assumed as adiabatic, therefore a zero gradient condition was set for the temperature. Table 1 shows the physical properties of the three fluids used for the simulation. Because of the expected Mach numbers and high temperature changes as a result of the adiabatic expansion the fluid is considered as compressible gas with a temperature dependent viscosity according to the Sutherland model. In the case of air and helium flow, the ideal gas equation was used, whereas for nitrogen the Peng-Robinson model was inserted.

The simulations of the MAS system were performed for different rotation frequencies f where the rotational speed was set to a constant value. The considered simulation cases are summarized in Table 2.

Table 2 Simulated cases

Diameter (mm)	Drive medium	Frequency (kHz)				CFD model
0.7	Air, 293 K	60	80	111	120	Ideal gas
1.3	Air, 293 K	23	55	67		Ideal gas
1.3	Nitrogen, 105 K	5	25	40		Peng Robinson
1.3	Helium, 45 K	20	55	67		Ideal gas

Table 3 Mach similarity for the same material and at a constant temperature, where $\rho, \dot{m}, c_p, \Delta T$ denote density, mass flow rate, heat capacity at constant pressure, and temperature difference, respectively (diameter d is variable)

Ma-similarity	$\mathrm{Ma}_1 = \mathrm{Ma}_2$	
Temperature	$T_1 = T_2$	
Sound velocity	$a_1 = a_2$	
Flow velocity	$U = \mathrm{Ma} \cdot a$	$U \sim 1$
Rotation rate	$f = U/(\pi \cdot d)$	$f \sim d^{-1}$
Mass flow rate	$\dot{m} = \rho \cdot U \cdot d^2$	$\dot{m} \sim d^2$
Pressure force	$F = \dot{m} \cdot U$	$F \sim d^2$
Pressure	$p = F/d^2$	$p \sim 1$
Torque	$M = \dot{m} \cdot U \cdot d/2$	$M \sim d^3$
Shaft power	$P_t = M \cdot 2 \cdot \pi \cdot f$	$P_t \sim d^2$
Mechanical power	$P_h = \dot{m} \cdot c_p \cdot \Delta T$	$P_h \sim d^2$
Efficiency	$\eta = P_t/P_h$	$\eta \sim 1$

2.5 Mach Similarity—Optimization Guidelines. The goal of this work is to provide a relevant contribution to the development of two new MAS product families. One MAS product family encompasses probes driven by air investigated at room temperature. The other one consists of low temperature MAS probes for 1.3 mm and 0.7 mm rotors driven by nitrogen, as well as 3.2 mm MAS helium probes. In addition, this work is a major contribution to the development of a scaling method, which can be used extensively for the development of new MAS probe types. They allow the rotor diameters, the temperature, and the medium to be scaled and provide information on the appropriate optimization, like nozzle diameter, nozzle position, blade number, etc.

Table 3 allows a view of how characteristic variables (such as rotational speed, torque, power, or efficiency) change as the geometry of the turbine is changed. Hereby, the Mach-similarity is shown for an ideal gas (i.e., $\mathrm{Ma}_1 = \mathrm{Ma}_2$) when the gas temperature is kept constant (i.e., $T_1 = T_2$), so that the sound velocity remains unchanged. In conclusion, the rotation rate changes inversely proportional to the probe rotor diameter; the mass flow rate and the power both change with diameter to the power of two; the torque changes with diameter to the power of three, but the turbine efficiency remains unchanged. Based on this Mach-similarity, in Tables 4 and 5, the changes in the rotation rate and mass flow are given for air and helium, respectively, which both can be considered as ideal gases.

Table 1 Simulation parameter values

Parameter	Unit	Air	Helium	Nitrogen
Heat capacity	J/(K m^3)	1005	5214	1141
Ambient pressure	bar	1	1	1
Ambient temperature	K	293	45	105
Sutherland coefficients	$\frac{\mathrm{kg}}{\mathrm{ms}\sqrt{\mathrm{K}}}$, K	1.48×10^{-5}, 116	1.1×10^{-6}, 10	1.39×10^{-6}, 106

Table 4 Mach similarity for air at a constant temperature

Diameter d (mm)	3.2	1.3	0.7
Rotation rate f (kHz)	27.22	67	124.43
Mass flow rate $\dot{m}$ (kg/s)	2.71×10^{-3}	4.47×10^{-4}	1.29×10^{-4}

Table 5 Mach similarity for He at a constant temperature

Diameter d (mm)	3.2	1.3
Rotation rate f (kHz)	8	19.69
Mass flow rate $\dot{m}$ (kg/s)	2.6×10^{-4}	4.29×10^{-5}

Table 6 Mach similarity for an ideal gas, same geometry, and at constant pressure, where κ and R denote the isentropic exponent and the specific gas constant (U, T are variable)

Ma-similarity	$\mathrm{Ma}_1 = \mathrm{Ma}_2$	
Geometry	$d_1 = d_2$	
Pressure	$p_1 = p_2$	
Sound velocity	$a = \sqrt{\kappa \cdot p/\rho} = \sqrt{\kappa \cdot R \cdot T}$	
Density	$\rho = p/(R \cdot T)$	$\rho \sim (R \cdot T)^{-1} \sim \kappa/a^2$
Flow velocity	$U = \mathrm{Ma} \cdot a$	$U \sim a$
Rotation rate	$f = U/(\pi \cdot d)$	$f \sim a$
Mass flow rate	$\dot{m} = \rho \cdot U \cdot d^2$	$\dot{m} \sim \rho \cdot a \sim \kappa/a$
Pressure force	$F = p \cdot d^2$	$F \sim 1$
Torque	$M = \dot{m} \cdot 2\pi f \cdot d^2/4$	$M \sim \kappa$
Shaft power	$P_t = M \cdot 2\pi f$	$P_t \sim \kappa \cdot a$
Mechanical power	$P_h = \dot{m} \cdot c_p \cdot \Delta T$	$P_h \sim \kappa/a \cdot c_p \cdot T = a \cdot c_p/R$
Efficiency	$\eta = P_t/P_h$	$\eta \sim \kappa \cdot R/c_p = R/c_v = \kappa - 1$

In contrast, Table 6 summarizes the characteristics of the microturbines relative to the characteristics of the drive medium (density, sound velocity, heat capacity, or isentropic exponent). Hereby, the Mach-similarity is shown for an ideal gas when the geometry and the driven pressure are kept constant (i.e., $d_1 = d_2, p_1 = p_2, \mathrm{Ma}_1 = \mathrm{Ma}_2$). In conclusion, the rotation rate changes proportionally to the sound velocity; the mass flow rate changes inverse proportionally to the sound velocity, the torque changes only relatively to the isentropic exponent, and the turbine efficiency is proportional to $1-\kappa$.

By means of these Mach-similarities, two important scaling methods are provided: Either measurement or simulation data from a MAS configuration can be transferred to a new one. These similarity techniques can be useful in providing optimization guidelines for a large MAS probe parameter range and even for other gas driven Pelton type turbines using different media.

In this work, we concentrate on the simulation of the MAS turbine system only. This approach has been chosen, in order to separate the effects of the turbine from the bearing flow system. It allows for an in-depth investigation of turbine flow dynamic but disregards feedback from the bearing onto the rotor. Hence, bearing induced flow instabilities, which are also important for the MAS probe head design are not taken into account. The CFD simulation method of our turbine is well established (cf. Wilhelm et al. [24], Herzog et al. [27]) for a 1.3 mm room temperature turbine system. This method is extended to a 0.7 mm room temperature case and 1.3 mm low temperature probes driven by cold nitrogen and helium. For the cold nitrogen case, real gas effects are thoroughly taken into account.

3 Results and Discussion

In this section, the flow dynamics of the MAS turbine system are investigated by analyzing the influence of rotational frequency and geometrical parameters on the microturbine efficiency. The efficiency of a MAS system is defined by the power delivered to the rotor (i.e., the shaft power) divided by the total power that depends mainly on the ratio of the supply pressure to the outlet pressure. It is aimed to reach a maximum rotational frequency at the lowest possible supply pressure. Since conventional compressed air systems have a certain pressure limitation, the inlet pressure required to drive the turbine should not exceed 5 bar. The rotational frequency is kept constant as mentioned before and thus the efficiency of the system is determined by the resulting drive torque on the turbine. With the assumption of constant bearing friction at a certain frequency the drive torque at the turbine allows for conclusions about the possible rotational speed.

3.1 Comparison of 0.7 mm and 1.3 mm Turbines. In the experiment, the inlet pressure is prescribed resulting in a respective mass flow. Whereas we prescribe the mass flow an inlet boundary condition for our CFD simulation, and a desired inlet pressure results. In Fig. 6(*a*) very good agreement between the measured and the simulated mass flow is seen for the 1.3 mm MAS system. However, for the 0.7 mm case the mass flow resulting from the simulation is about 36% lower than in the experiment. This is a direct consequence of the fabrication tolerance of the nozzle. Note that the relative inflow pressure is computed by drive pressure minus outflow pressure (which is equal to 1 bar, i.e., ambient conditions).

3.2 Power and Efficiency Factor. For comparison with experimental measurements, the MAS turbine efficiency is defined by the following relation:

$$\eta = \frac{P_{\mathrm{shaft}}}{P_{\mathrm{total}}} \tag{4}$$

The total power P_{total} can be defined by means of the work of an adiabatic process and the mass flux $\dot{m}$

$$P_{\mathrm{total}} = \dot{m}\, c_p\, T_1 \left[1 - \left(\frac{p_2}{p_1}\right)^{\frac{\kappa-1}{\kappa}}\right] \tag{5}$$

where c_p is the specific heat capacity, T_1 is the absolute temperature, p_1 is the absolute static pressure at the inlet (supply pressure), p_2 is the outlet pressure, an κ is the isentropic exponent. Here we neglected the velocity at the outflow. The shaft power is defined by

$$P_{\mathrm{shaft}} = \omega M_z \tag{6}$$

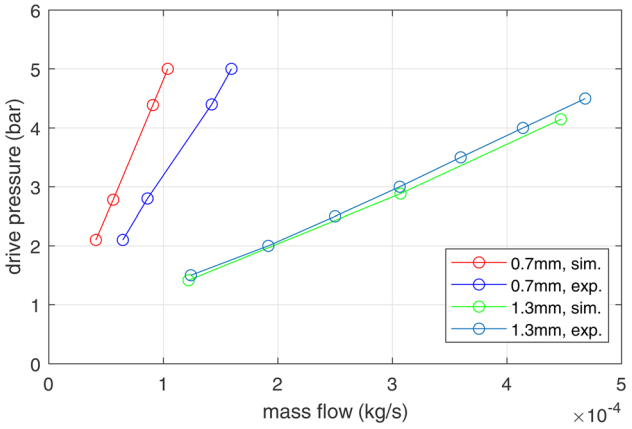

Fig. 6 Drive pressure as a function of mass flow—comparison between simulation and experiment with function pattern

Table 7 Drive torque about *z*-axis for MAS 0.7 mm

Rotation rate (kHz)	Inflow pressure relative (bar)	Mass flow $(kg/s) \cdot 10^{-5}$	Pressure component $(N \cdot m) \cdot 10^{-6}$	Shear component $(N \cdot m) \cdot 10^{-8}$	Driven torque $(N \cdot m) \cdot 10^{-6}$	Ratio of shear and pressure component (%)
60	1.1	4.11	1.553	−4.120	1.512	−2.65
80	1.8	5.62	2.056	−6.441	1.991	−3.13
111	3.4	9.09	2.630	−9.920	2.531	−3.77
120	4.0	10.38	2.731	−10.790	2.623	−3.95

In Eq. (6) the drive torque about the z-axis is computed from the pressure and the shear component acting on the turbine blades. Table 7 summarizes these components for the different rotation rates considered and Fig. 7 shows the respective torque values.

The shaft power, computed from the torque, drives the rotor, and it is converted into friction power inside the two bearings and on the surface of the rotor (due to gas viscosity). Thus, we denote the sum of bearing power and surface friction power as friction power P_{friction}. The friction energy is essentially converted into heat.

Consequently, the temperature increase can be used to calculate the friction power

$$P_{\text{friction}} = \dot{m} \left(c_p \cdot \Delta T + \frac{|u_2|^2}{2} \right) \tag{7}$$

where ΔT and u_2 denote the temperature difference between inlet and outlet, and the exit velocity at the outlet, respectively.

If we neglect the velocity of the fluid, we can compute the friction power directly from the temperature change ΔT. Corresponding temperature changes were measured using a thermal imaging camera on the 1.3 mm system.

Figure 8 shows a thermal camera image of the 1.3 mm rotor revolving at a frequency of 67 kHz. In horizontal and vertical direction the number of pixels are given in the graph. For orientation, we marked the rotor region in the sketch from Fig. 2 red and depicted this region in the thermal camera image. The photo in Fig. 8(*d*) illustrates the rotor region, which is recorded by the thermal camera. It is clearly visible that the rotor is the hottest region of the MAS turbine system, which is heated up due to air friction. In order to evaluate the temperature difference ΔT, we subtracted the background temperature, obtained from a rotor without rotation, from the camera image, see Figs. 8(*a*) and 8(*b*), respectively. Additionally, ΔT is computed by averaging over the pixels representing the hottest region of the rotor (i.e., the bright yellow points in the center of the red rectangle). It can be seen that the temperature difference is 30 °C for the 1.3 mm rotor at a rotation frequency of 67 kHz. This is in good agreement with the simulation results of the same case described by Wilhelm et al. [24].

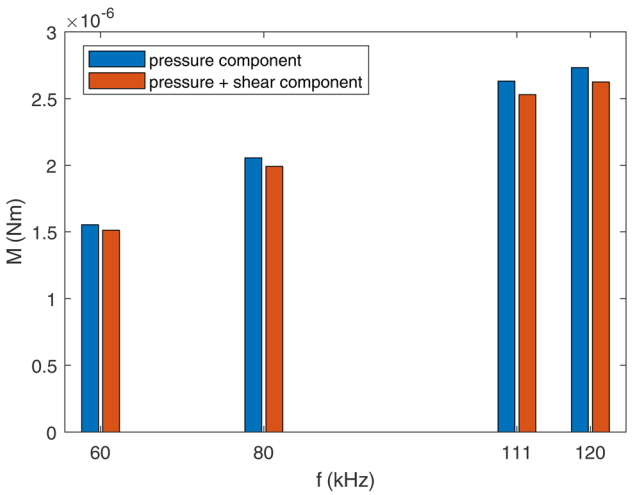

Fig. 7 Torque about the *z*-axis for MAS 0.7 mm

Moreover, it is also possible to determine the sample temperature change by a dedicated NMR experiment. We assume a measurement uncertainty in the temperature values of about ±10% for both methods. The main reason is that both the thermal images and the NMR experiment give only local temperature information. In Figure 9 both methods are used, where the temperature changes of the 1.3 mm and 0.7 mm system are plotted as a function of the rotation speed (air at ambient temperature). It is seen that the thermal imaging results agree quite well with the NMR results for the 1.3 mm MAS system.

Figure 10 shows the measured friction power as a function of the rotation frequency compared to the shaft power obtained from the CFD simulations. We observe lower experimental values of the friction power for the 1.3 mm system compared to the simulation results. This might be due to in-stationary effects or to a not vanishing exit velocity u_2 in the present case. However, for the 0.7 mm MAS system, we observe a fairly good agreement between shaft power and bearing power, which is deduced from NMR results only. These two completely independent measurement methods together are a good indication for the assumption that the major part of the shaft power is converted into friction power, furthermore, the friction energy is essentially converted into heat. Moreover, the measurement results serve as a validation of our numerical simulations, taking the mentioned measurement uncertainty of ±10% into account. We conclude that the shaft power of a 1.3 mm and a 0.7 mm turbine is 6.6 W (at $f = 67$ kHz) and 2 W (at $f = 120$ kHz), respectively. To our knowledge, this is the first experimental validation of shaft power values for 1.3 mm and 0.7 mm MAS systems.

Having the shaft power values at hand, we can easily compute the turbine efficiency. Tables 8, 9, and Fig. 11 show the efficiency of both MAS systems. It is interesting to note that the efficiency decreases with the rotation speed for both systems and the 0.7 mm MAS system exhibits a higher efficiency for all rotation speeds. This contrasts with the scaling of Table 3, which predicts a constant efficiency when scaling the rotor diameter d. However, due to fabrication restrictions, not all geometry parameters are identically scaled. Moreover, we have considered the optimization guidelines of Herzog et al. [27] for the 0.7 mm turbine system design, i.e., the number of blades has been increased (from 4 to 5), the scaled nozzle diameter has been reduced and the number of nozzles has been increased (from 7 to 8). Although efficiency is forehand not the main optimization parameter for MAS turbine design, higher efficient turbines need a smaller pressure difference (or mass flow) in order to reach the same rotation frequency. This is important for low temperature MAS systems, where costly low temperature media (cooled nitrogen or helium) are employed as drive gas.

3.3 Geometry Optimization of the Rotor-Stator System at Low Temperature. The optimizations or simulations were carried out with the media nitrogen (at a temperature of 105 K) and helium (at a temperature of 45 K). For helium, the ideal gas equation could be used as the state equation at the existing operating pressures and temperatures. The deviation from real gas is less

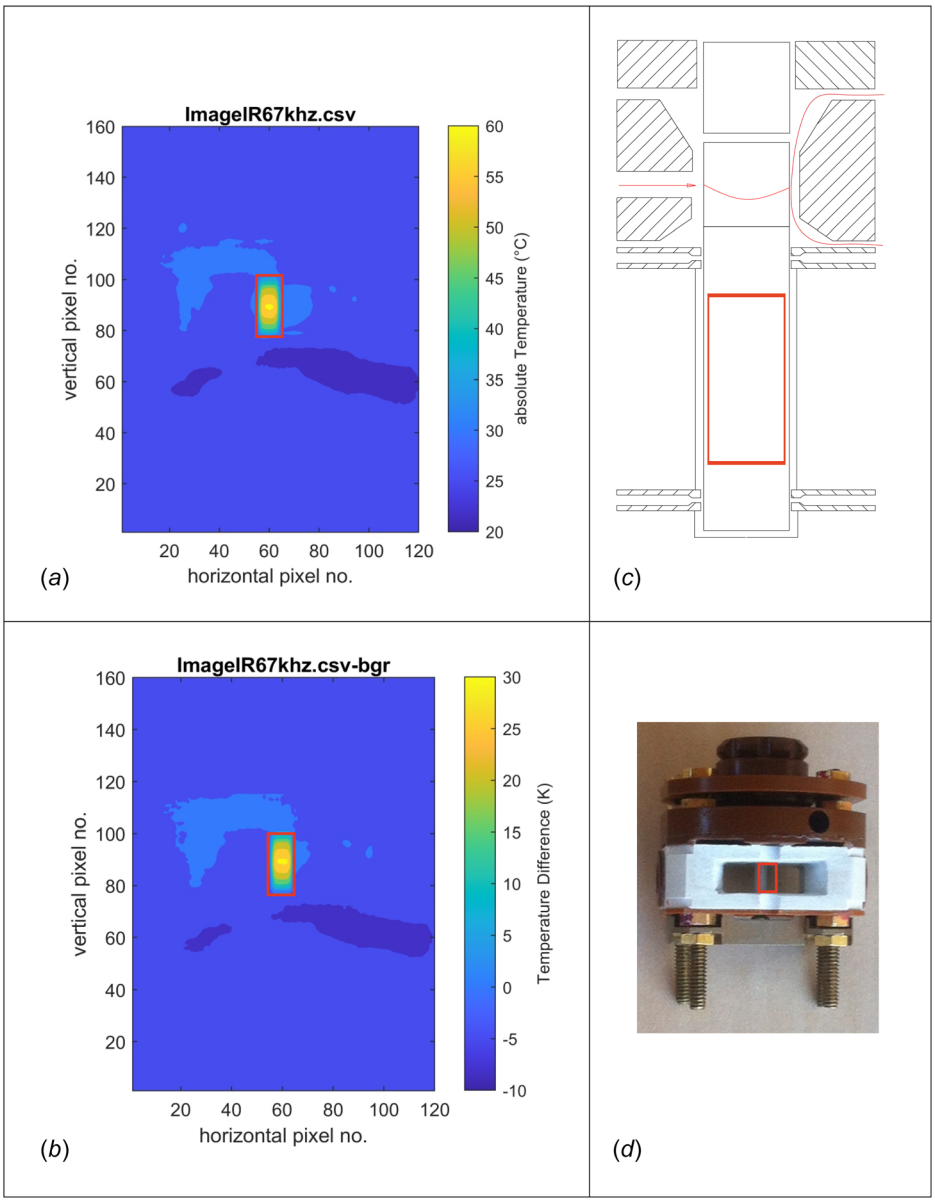

Fig. 8 (*a*) Thermal camera image of 1.3 mm MAS rotor system (scale in °C) with rotation frequency of 67 kHz and (*b*) difference temperature of background and values from (*a*). (*c*) Sketch of MAS rotor system illustrating the relevant region by the red square in (*a*) and (*b*). (*d*) Photo of MAS turbine system with relevant rotor region marked red.

than 1% and therefore negligible. For nitrogen, the deviation between ideal gas law and real gas is up to 8%. Therefore, the state equation according to Peng–Robinson was used for the simulation.

For helium, pressure as a function of the mass flow agrees very well with the curve of air at room temperature (see Fig. 12). For this purpose, the density of the media has a significant influence which is approximately the same at the operating points 45 K for helium and room temperature for air. With nitrogen as the driving medium, the situation is different. Nitrogen at 105 K has about a factor of three higher density, while the viscosity is half compared to air at room temperature. Both properties lead to a lower pressure difference at the same mass flow (Fig. 12).

Figure 13 shows the torque of the rotor to be applied to the three media. The torque for nitrogen is higher at a comparable speed than that for air, because of the higher density. With helium, the torque is comparable to air (comparable speeds and densities). The present results clearly show that the relation of mass flow to drive pressure is very similar for air at room temperature and helium at very low temperature (45 k). Furthermore, the torque that is delivered by the turbine is comparable for ambient air and cold helium, but higher for cold nitrogen. Hence, the design of low temperature helium MAS systems can easily be adapted from room temperature air system designs. In contrast, this is not the case for low temperature nitrogen systems (at 105 K), which reach the same mass flow with a smaller drive pressure and a higher torque at the same rotation frequency.

We compare the efficiency for these three media in Fig. 14. Here, the helium case shows the highest efficiency. However, frequency and efficiency are quantities that depend on the medium. Hence, in the next step, we scaled the helium and nitrogen case to that of ambient air. Therefore, the frequency f is scaled according to Table 6, i.e., by the speed of sound and the efficiency is scaled by $\kappa - 1$. Now the ambient air case exhibits the highest efficiency followed by the nitrogen case and the helium case is least efficient (which is due to the significant higher κ), cf. Fig. 15. Moreover, it

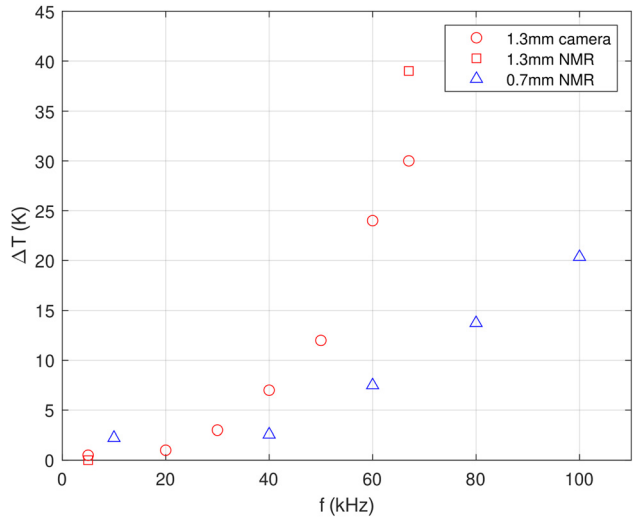

Fig. 9 Heating of the sample as a function of the rotating speed. Results from thermal imaging (camera) and dedicated NMR experiment (NMR).

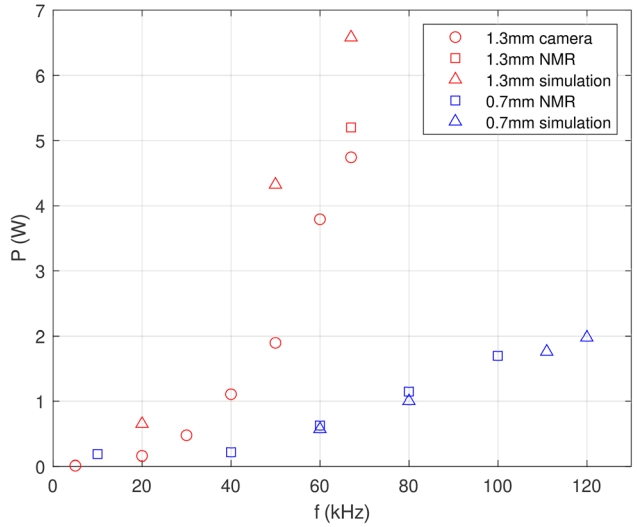

Fig. 10 Comparison of shaft and friction power between experiment and simulation for 1.3 mm and 0.7 mm case

Table 8 Efficiency factor for MAS 0.7 mm (simulation results)

Rotation rate (kHz)	P_{shaft} (W)	P_{total} (W)	Efficiency factor
60	0.57	2.32	0.25
80	1.00	4.20	0.24
111	1.76	9.25	0.19
120	1.98	11.31	0.17

Table 9 Efficiency factor for MAS 1.3 mm (simulation results)

Rotation rate (kHz)	P_{shaft} (W)	P_{total} (W)	Efficiency factor
23	0.65	3.40	0.19
55	4.32	23.68	0.18
67	6.58	44.09	0.15

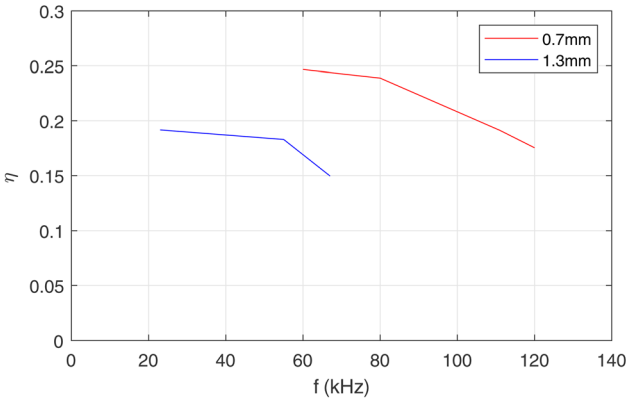

Fig. 11 Turbine efficiency as a function of the speed—comparison of the 0.7 mm against the 1.3 mm system

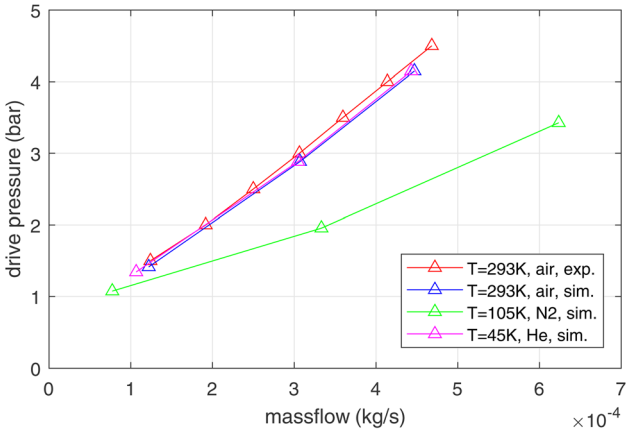

Fig. 12 Drive pressure as a function of the mass flow for the media air at room temperature, nitrogen at 105 K, and helium at 45 K

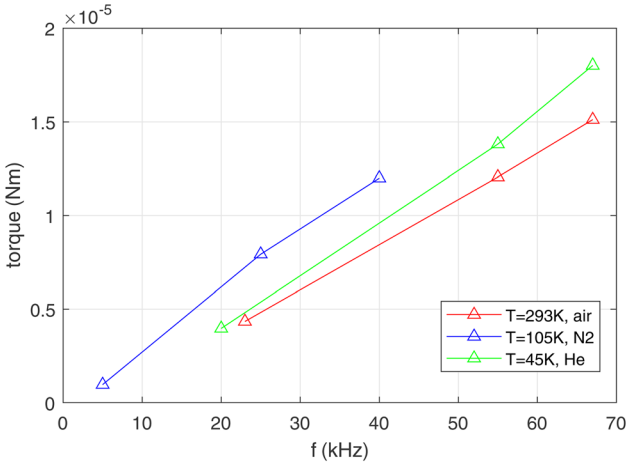

Fig. 13 Torque of the rotor in speed equilibrium for air, nitrogen, and helium

is seen that all scaled frequencies are in the same range of about 10–70 kHz. Table 10 summarizes the thermodynamic properties used for the scaling, where the max. rotation rate is calculated assuming to be 80% of the respective speed of sound (i.e., the outer rotor wall rotates with a velocity of $2\pi f\, r = 0.8\, a$).

At the available pressures and temperatures, nitrogen has a sound velocity that is about 40% lower than that of air.

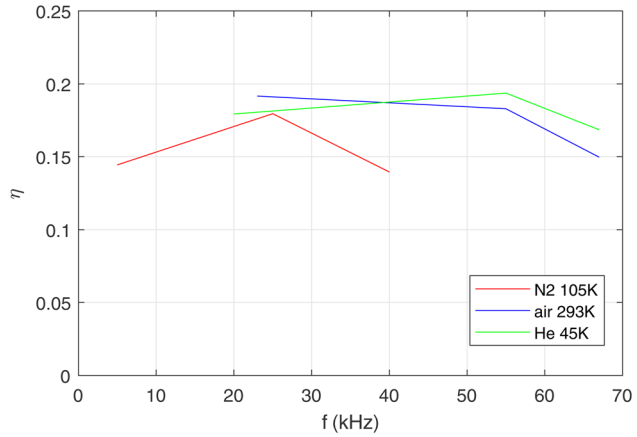

Fig. 14 Efficiency as a function of speed for air, nitrogen, and helium

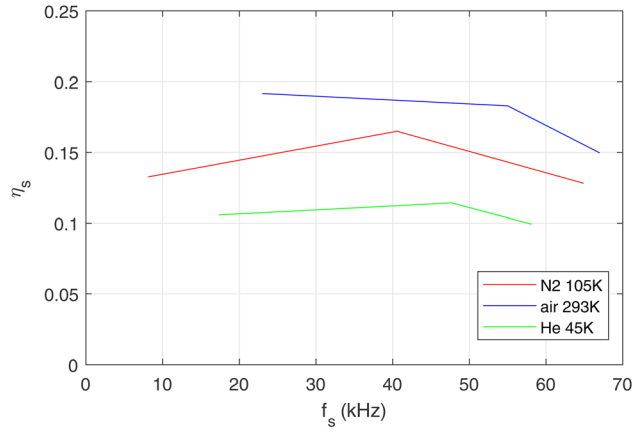

Fig. 15 Efficiency of helium and nitrogen scaled to ambient air case (i.e., $f \sim a, \eta \sim \kappa - 1$)

Table 10 Mach similarity for same geometry, varying temperature and gas

Gas	Air	Nitrogen	Helium
Temperature T (K)	293	105	45
Sound velocity a (m/s)	342.6	211.1	395.1
Max. rotation rate f (kHz)	67.1	41.4	77.4
Specific gas constant R (J/(kg·K))	287.1	296.84	2077.1
Isentropic exponent κ	1.395	1.43	1.67
Real gas coefficient Z	1	0.9	1

The max. rotation rate is referred to as 80% of the respective speed of sound.

Considering the Mach number in the region of the nozzle, it can be seen that for increasing frequency the Mach number stays below 0.8. In Fig. 16(*a*) cut through the 1.3 mm turbine at nozzle level is shown for rotation frequency of 67 KHz. In this contour plot, the nozzle cross section is marked of which an average Mach number is computed. The right figure shows the Mach number averaged over this nuzzle region as a function of the rotation frequency for ambient air, cold nitrogen, and cold helium. Inside the smallest cross section subsonic conditions prevail before the fluid flow is expanded in the rotor region. It is seen that the Mach number approaches a maximum of about 0.8. Hence, we conclude from this that for our nozzle turbine combination a Mach number limit of about 0.8 is applicable. Therefore, a 1.3 mm nitrogen turbine could reach a frequency of about 40 kHz and a helium system of about 77 kHz (cf. Table 10). It is an important conclusion for the MAS turbine system design that the rotation frequency is limited by about 80% of the Mach number. Consequently, high rotation speed can be achieved only by successively decreasing the rotor diameter, which is very demanding from a fabrication point of view.

As in Sec. 3.2, we consider the shaft power for ambient air and helium (45 K) case, see Fig. 17. Simulation results are compared with the friction power deduced from thermal camera images (cf. Sec. 3.2). According to Petroff's equation [39], the bearing power is a quadratic function of the frequency. A quadratic fit of the simulation values is introduced in the graph. It is clearly seen that the results for all three cases, i.e., ambient air, low temperature helium, and nitrogen, follow the quadratic law given by the fitting curve. We conclude that the turbine power follows the same quadratic role over a wide temperature range of 45 K to 293 K, employing different drive media.

3.4 Prototyping and Optimization of the Low-Temperature Rotor-Stator System. Due to the optimized design, a low temperature prototype probe was built by Bruker. This prototype was tested experimentally and the results were compared with the simulation results (Fig. 18). The focus here is on the flow-mechanical and thermodynamic behavior.

The prototype was run at a sample temperature of 25–55 K. In typical NMR applications, large radio frequency (RF) fields are required for the measurement. This leads to high electrical voltages in the probe. Thus, the resistance of helium against electrical breakthrough (ionization avalanches) was also experimentally tested at low temperatures. Furthermore, the RF part of the probe was optimized geometrically to withstand the RF voltage strength, which has a positive effect on the signal-to-noise ratio.

The probe is used for DNP experiments (see, e.g., Ref. [36]), which is a special type of NMR experiment. Figure 19 shows the DNP gain for nitrogen probes (105 K) and helium probes (60 K) as a function of the gyrotron collector current, the latter being proportional to the microwave power applied. The helium probe achieves approximately 50% higher amplification values.

The flow-mechanical comparison between experiment and simulation shows good agreement for all three media air, nitrogen, and helium at low temperature. The experiments with helium at low temperature were carried out on a 3.2 mm MAS system and then scaled to the 1.3 mm system for comparability. It can also be seen here that the scaling methods developed in Sec. 2.5 provide good accuracy. In this way, knowledge and data from one MAS system can reliably be mapped to another system, with regard to geometry and media or temperatures. Figure 18 depicts drive pressure as a function of mass flow for the following simulation cases: 1.3 mm turbine system driven with cold helium, cold nitrogen, and ambient air. These simulations are compared with experimental results from 1.3 mm turbine systems also driven by cold nitrogen and ambient air, as well as results of a 3.2 mm turbine system driven by cold helium. The presented scaling approach allows for comparison of the 3.2 mm hardware system with simulations of a 1.3 mm case. Since the fabrication of an NMR probe head is rather costly, it is very helpful if existing measurement results and simulation results can be scaled over a larger geometry and temperature range. The scaling can also be employed to speed up the development and design phase since it enables the reuse of existing results. Moreover, the scaling approach can be employed to a wider class of microturbine systems that operate over a large temperature range employing different working media.

4 Conclusion

In this work, the flow dynamics of a high speed microturbine system are investigated numerically utilizing CFD simulations with the open source tool OpenFOAM for a wide temperature

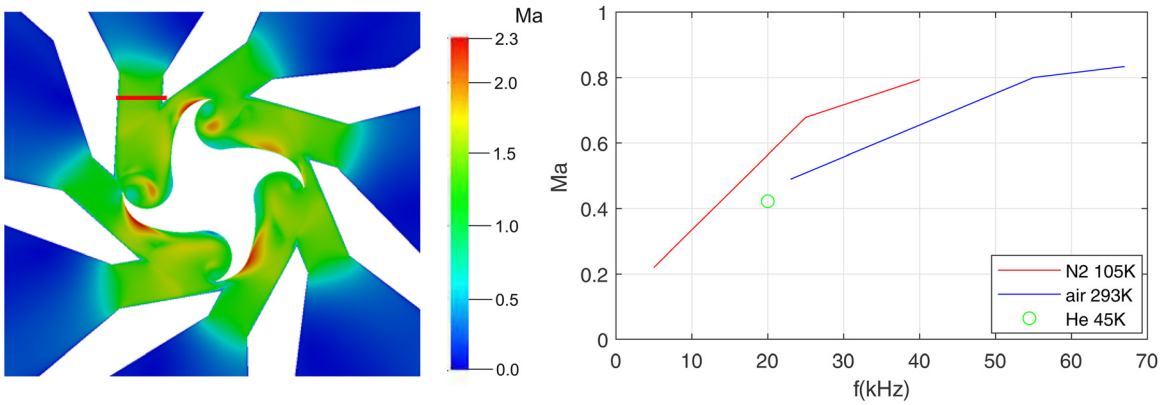

Fig. 16 Left: red bar marks nozzle region, where the Mach number is evaluated, a figure of 1.3 mm turbine, ambient air at $f = 67$ kHz. Right: average of Mach number in the nozzle region (as marked left) for different media as a function of the rotation frequency.

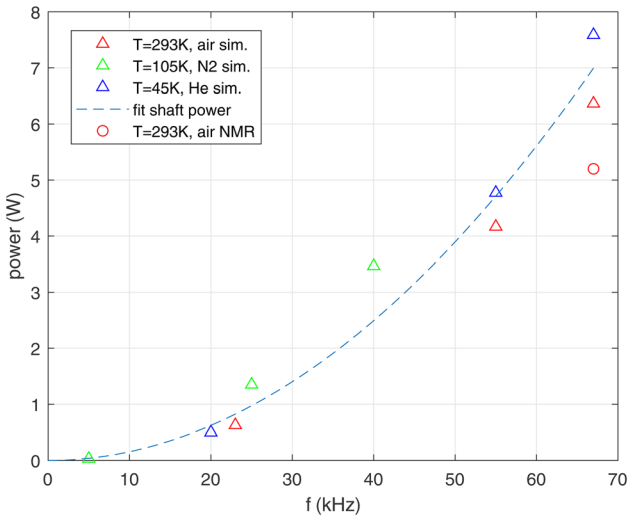

Fig. 17 Comparison of the shaft power and friction power between experiment and simulation for 1.3 mm case and different temperatures

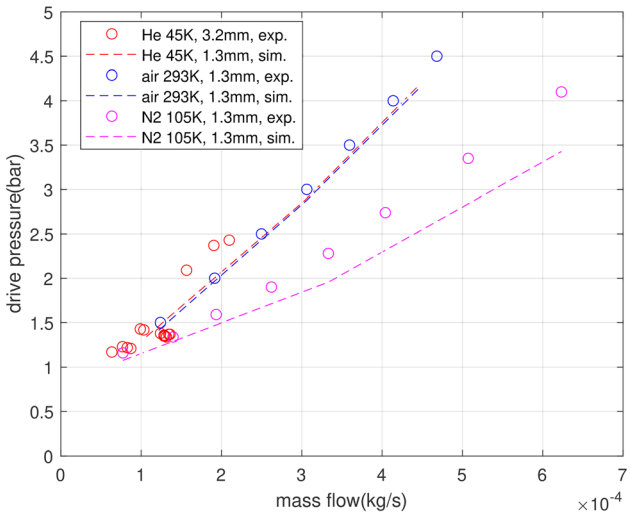

Fig. 18 Drive pressure as a function of mass flow, MAS 1.3 mm, air at 293 K, nitrogen at 105 K, He at 45 K—comparison experiment and simulation. Experiment with He at 45 K on MAS 3.2 mm scaled to MAS 1.3 mm.

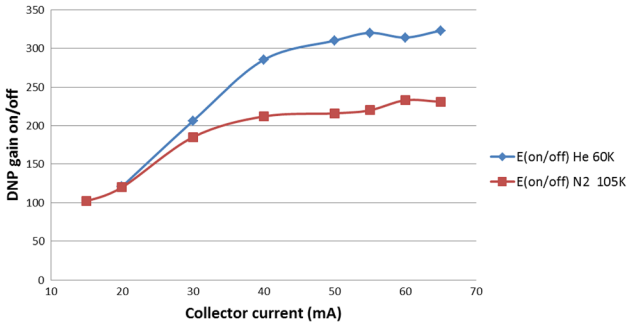

Fig. 19 NMR DNP experiment: DNP amplification at HeMAS at 60 K compared to 105 K N2

range of 45 K to 293 K. Three different media are investigated: air, nitrogen, and helium. CFD results are presented and compared with measurements of the microturbine for a rotor diameter of 1.3 mm and 0.7 mm.

A blade turbine is driven by compressed air, nitrogen, or helium at which the gas is jetted out through duct nozzles positioned on an intake spiral. Rotation frequencies of 20 kHz up to 120 kHz are considered. The microturbine system is investigated by analyzing the influence of rotational frequency and geometrical parameters on the aerodynamic forces and torque and the turbine efficiency.

To our knowledge, the first comprehensive microturbine studies for such a large temperature range, i.e., ultralow temperature of 45 K up to ambient temperature, is presented. It is shown that liquid helium driven microturbines at 45 K behave very similar to air driven microturbines at ambient temperature. Typically drive pressure and flow rates show the same relation for low temperature helium and ambient air. This is confirmed by experimental and simulation results. On the other hand, nitrogen at 105 K has a threefold higher density and much lower viscosity than air at room temperature. Both factors lead to a lower mass flow to be applied for the same rotation speed of the turbine. It is shown that the maximum local Mach number in the nozzles is about 0.8. This results in a lower maximal rotation speed of the low temperature nitrogen system, due to the lower speed of sound of nitrogen at 105 K. Moreover the efficiency of the nitrogen system is lower than for the helium and the ambient air systems.

All simulations are performed with laminar solvers due to earlier investigations on similar MAS turbine configurations that showed very small influences of the turbulence models. We used ideal gas models for ambient air and ultralow temperature helium. Nitrogen (at 105 K) is modeled employing a Peng–Robinson model to cope with real gas effects.

As regards the efficiency of our microturbines, all of them are designed with the goal to reach maximum rotation speed. Efficiency is a parameter, although important, which however is subordinated relative to turbine speed. Going from a larger rotor diameter, e.g., 1.3 mm, to a smaller one, e.g., 0.7 mm, or changing temperatures over a wide range, or using different fluids to operate the MAS system (nitrogen, air, helium) requires several design conditions to be satisfied: (i) limiting the centrifugal forces on the rotor wall materials proportional to the rotor radius and the square of the angular velocity, (ii) making sure that the fluid dynamics of the turbine for various gases and at various temperatures works properly—the topic of this paper, (iii) adapting the numbers of turbine nozzles (number and diameter), and (iv) optimizing the shape and the number of turbine blades. The relevance of our study and its results as presented in this paper lies in providing a framework resulting in the fluid dynamics insofar that the similarity relations (Tables 3–6) can be verified and gas pressures and mass flow rates, in particular for the 0.7 mm system, lie in a technically and practically feasible range. With that fluid dynamics framework in place, we can focus on design parameters like the turbine geometry.

In this work, prototype systems have been fabricated and tested for all investigated configurations, i.e., ultralow temperature helium turbine, low temperature nitrogen turbine, and ambient air temperature systems for different diameters. The experimental results are in good agreement with simulations. Furthermore, low temperature prototypes are tested for their main applications of DNP experiments.

Funding Data

- Commission for Technology and Innovation (Project KTI-Nr. 17247.1 PFIW-IW; Funder ID: 10.13039/501100001808).

References

[1] Zhou, T., Xu, Y., Liu, Z., and Joo, S. W., 2015, "An Enhanced One-Layer Passive Microfluidic Mixer With an Optimized Lateral Structure With the Dean Effect," ASME J. Fluids Eng., **137**(9), p. 091102.

[2] Mäki, A.-J., Hemmilä, S., Hirvonen, J., Girish, N. N., Kreutzer, J., Hyttinen, J., and Kallio, P., 2015, "Modeling and Experimental Characterization of Pressure Drop in Gravity-Driven Microfluidic Systems," ASME J. Fluids Eng., **137**(2), p. 021105.

[3] Solovitz, S. A., Zhao, J., Xuem, W., and Xu, J., 2013, "Uniform Flow Control for a Multipassage Microfluidic Sensor," ASME J. Fluids Eng., **135**(2), p. 021101.

[4] Sharp, K., 2013, "Editorial for the Special Issue on Microfluidics," ASME J. Fluids Eng., **135**(2), p. 020201.

[5] Lee, C., Arslan, S., Luc, G., and Fréchette, L., 2008, "Design Principles and Measured Performance of Multistage Radial Flow Microturbomachinery at Low Reynolds Numbers," ASME J. Fluids Eng., **130**(11), p. 111103.

[6] Epstein, A., and Senturia, S., 1997, "Macro Power From Micro Machinery," Science, **276**(5316), pp. 1211–1211.

[7] Fréchette, L. G., Lee, C., Arslan, S., and Liu, Y.-C., 2003, "Design of a Microfabricated Rankine Cycle Steam Turbine for Power Generation," ASME Paper No. IMECE2003-42082.

[8] Liamini, M., Shahriar, H., Vengallatore, S., and Fréchette, L. G., 2011, "Design Methodology for a Rankine Microturbine: Thermomechanical Analysis and Material Selection," J. Microelectromech. Syst., **20**(1), pp. 339–351.

[9] Lee, C., and Fréchette, L., 2011, "A Silicon Microturbopump for a Rankine-Cycle Power Generation Microsystem-Part I: Component and System Design," J. Microelectromech. Syst., **20**(1), pp. 312–325.

[10] Fréchette, L. G., Jacobson, S., Breuer, K., Ehrich, F., Ghodssi, R., Khanna, R., Wong, C., Zhang, X., Schmidt, M., and Epstein, A. H., 2005, "High-Speed Microfabricated Silicon Turbomachinery and Fluid Film Bearings," J. Microelectromech. Syst., **14**, pp. 141–152.

[11] Ribaud, Y., Dessornes, O., Guidez, J., Courvoisier, T., Dumand, C., Kozanecki, Z., Helin, P., Moal, P., and Minotti, P., 2005, "The Experience Gained on the Ultra Microturbine: From Energetics to Component Brick Studie," Power-MEMS,Tokyo, Nov. 28-30, pp. 21–24.

[12] Philippon, B., 2001, "Design of a Film Cooled Mems Micro Turbine," Ph.D. thesis, Massachusetts Institute of Technology, Cambridge, MA.

[13] Dessornes, O., Landais, S., Valle, R., Fourmaux, A., Burguburu, S., Zwyssig, C., and Kozanecki, Z., 2013, "Advandes in the Development of Micro-Turbine Engine at Onera," ASME Paper No. GT2013-94005.

[14] Lin, S., Daze, C., Davis, M., Cague, T., LaRochelle, M., Kidane, R., Lessa, L., Slate, D., and Kozak, J., 2004, "Micro Turbine Development," KGCOE-MD2004 Multi-Disciplinary Engineering Design Conference, Rochester, NY, May, MD2004-04013.

[15] Vézina, G., Frotier-Topping, H. F., Bolduc-Teasdale, F., Rancourt, D., Picard, M., Plante, J.-S., Bourillete, M., and Fréchette, L., 2016, "Design and Experimental Validation of a Supersonic Concentric Micro Gas Turbine," ASME J. Turbomach., **138**, p. 021007.

[16] Blümich, B., 2005, *Essential NMR: For Scientists and Engineers*, Springer, Berlin, Germany.

[17] Ernst, R., Bodenhausen, G., and Wokaun, A., 1989, *Principles of Nuclear Magnetic Resonance in One and Two Dimension*, Oxford Univ. Press, New York.

[18] Keeler, J., 2007, *Understanding NMR Spectroscopy*, Wiley, Chichester, UK.

[19] Doty, F., 1996, "Solid State Probe Design," *Encyclopedia of Nuclear Magnetic Resonance*, D. Grant and R. Harris, eds., Wiley, Chichester, pp. 4475–4485.

[20] Samoson, A., 2002, "Extended Magic-Angle Spinning," *Encyclopedia of Nuclear Magnetic Resonance*, D. Grant and R. Harris, eds., Vol. 9, Wiley, Chichester, UK, pp. 59–64.

[21] Doty, F., and Ellis, P., 1981, "Design of High-Speed Cylindrical NMR Sample Spinners," Rev. Sci. Instrum., **52**(12), pp. 1868–1875.

[22] Doty, F., Miller, B., Hosford, G., Wilson, D., and Jones, J., 1991, "High Efficiency Microturbine Technology," 26th Intersociety Energy Conversion Engineering Conference, Boston, MA, Aug. 4-9, pp. 436–442

[23] Matsuki, Y., Ueda, K., Idehara, T., Ikeda, R., Ogawa, I., Nakamura, S., Toda, M., Anai, T., and Fujiwara, T., 2012, "Helium-Cooling and Spinning Dynamic Nuclear Polarization for Sensitivity-Enhanced Solid-State Nmr at 14T and 30 K," J. Magn. Reson., **225**, pp. 1–9.

[24] Wilhelm, D., Purea, A., and Engelke, F., 2015, "Fluid Flow Dynamics in Mas Systems," J. Magn. Reson., **257**, pp. 51–63.

[25] Lakomek, N.-A., Penzel, S., Lends, A., Cadalbert, R., Ernst, M., and Meier, B. H., 2017, "Microsecond Dynamics in Ubiquitin Probed by Solid-State NMR 15n r1rho Relaxation Experiments Under Fast Mas (60–110 Khz)," Chem.-A Eur. J., **23**(39), pp. 9425–9433.

[26] Sesti, E. L., Alaniva, N., Rand, P. W., Choi, E. J., Albert, B. J., Saliba, E. P., Scott, F. J., and Barnes, A. B., 2018, "Magic Angle Spinning Nmr Below 6 K With a Computational Fluid Dynamics Analysis of Fluid Flow and Temperature Gradients," J. Magn. Reson., **286**, pp. 1–9.

[27] Herzog, N., Wilhelm, D., Koch, S., Purea, A., Osen, D., Knott, B., and Engelke, F., 2016, "Aerodynamic Optimization of a Microturbine Inserted in a Magic-Angle Spinning System," ASME J. Fluids Eng., **138**(12), p. 121106.

[28] Chen, P., Albert, B. J., Gao, C., Alaniva, N., Price, L. E., Scott, F. J., Saliba, E. P., Sesti, E. L., Judge, P. T., Fisher, E. W., and Barnes, A. B., 2018, "Magic Angle Spinning Spheres," Sci. Adv., **4**(9), p. eaau1540.

[29] Chen, P.-H., Gao, C., and Barnes, A. B., 2019, "Perspectives on Microwave Coupling Into Cylindrical and Spherical Rotors With Dielectric Lenses for Magic Angle Spinning Dynamic Nuclear Polarization," J. Magn. Reson., **308**, p. 106518.

[30] Osborn Popp, T. M., Däpp, A., Gao, C., Chen, P.-H., Price, L. E., Alaniva, N. H., and Barnes, A. B., 2020, "Highly Stable Magic Angle Spinning Spherical Rotors," Magn. Reson., **1**(1), pp. 97–103.

[31] Chen, N., 2010, *Aerothermodynamics of Turbomachinery: Analysis and Design*, Wiley, Singapore, Singapure

[32] Logan, E., and Roy, R., 2003, *Handbook of Turbomachinery*, Marcel Dekker, New York.

[33] Rosay, M., Tometich, L., Pawsey, S., Bader, R., Schauwecker, R., Blank, M., Borchard, P. M., Cauffman, S. R., Felch, K. L., Weber, R. T., Blank, M., Borchard, P. M., Cauffmann, S. R., Felch, K. L., Weber, R. T., Temkin, R. J., Griffin, R. G., and Maas, W. E., 2010, "Solid-State Dynamic Nuclear Polarization at 263 Ghz: Spectrometer Design and Experimental Results," Phys. Chem. Chem. Phys., **12**(22), pp. 5850–5860.

[34] Ni, Q. Z., Markhasin, E., Can, T. V., Corzilius, B., Tan, K. O., Barnes, A. B., Daviso, E., Su, Y., Herzfeld, J., and Griffin, R. G., 2017, "Peptide and Protein Dynamics and Low-Temperature/DNP Magic Angle Spinning NMR," J. Phys. Chem. B, **121**(19), pp. 4997–5006.

[35] Maly, T., Debelouchina, G. T., Bajaj, V. S., Hu, K.-N., Joo, C.-G., Mak-Jurkauskas, M. L., Sirigiri, J. R., van der Wel, P. C., Herzfeld, J., Temkin, R. J., and Griffin, R. G., 2008, "Dynamic Nuclear Polarization at High Magnetic Fields," J. Chem. Phys., **128**(5), p. 052211.

[36] Lee, D., Bouleau, E., Saint-Bonnet, P., Hediger, S., and De Paëpe, G., 2016, "Ultra-Low Temperature MAS-DNP," J. Magn. Reson., **264**, pp. 116–124.

[37] Hillewaert, K., and van den Braembussche, R., 2000, *Comparison of Frozen Rotor to Unsteady Calculations of Incompressible Turbomachinery Flow*, Proceedings of the 5th National Congress on Theoretical and Applied Mechanics, Louvain-la-Neuve, Belgium, pp. 335–338

[38] Vuorinen, V., Keskinen, J.-P., Duwig, C., and Boersma, B., 2014, "On the Implementation of Low-Dissipative Runge-Kutta Projection Methods for Time Dependent Flows Using Openfoam," Comput. Fluids, **93**, pp. 153–163.

[39] Smith, S. R., Hamrock, B. J., and Jacobson, B. O., 2014, *Fundamentals of Machine Elements*, CRC Press, Boca Raton, FL